Mesoscopic finite-size effects of unconventional electron transport in math xmlns="http://www.w3.org/1998/Math/MathML">msub>mi mathvariant="normal">PdCoO/mi>mn>2/mn>/msub>/ma th>

Georgios Varnavides, Yaxian Wang, Philip J. W. Moll, Polina Anikeeva, and Prineha Narang

Mesoscopic finite-size effects of unconventional electron transport in PdCoO$_2$

Georgios Varnavides,[1,2,3,*] Yaxian Wang,[1,*] Philip J.W. Moll,[4] Polina Anikeeva,[2,3] and Prineha Narang[1,†]

[1]*John A. Paulson School of Engineering and Applied Sciences, Harvard University, Cambridge, MA 02138, USA*
[2]*Department of Materials Science and Engineering, Massachusetts Institute of Technology, Cambridge, MA 02139, USA*
[3]*Research Laboratory of Electronics, Massachusetts Institute of Technology, Cambridge, MA 02139, USA*
[4]*Laboratory of Quantum Materials (QMAT), Institute of Materials (IMX),*
ÃĽcole Polytechnique FÃĺdÃĺrale de Lausanne (EPFL), 1015 Lausanne, Switzerland
(Dated: March 17, 2022)

A wide range of unconventional transport phenomena have recently been observed in single-crystal delafossite metals. Here, we present a theoretical framework to elucidate electron transport using a combination of first-principles calculations and numerical modeling of the anisotropic Boltzmann transport equation. Using PdCoO$_2$ as a model system, we study different microscopic electron and phonon scattering mechanisms and establish the mean free path hierarchy of quasiparticles at different temperatures. We treat the anisotropic Fermi surface explicitly to numerically obtain experimentally-accessible transport observables, which bridge between the "diffusive", "ballistic", and "hydrodynamic" transport regime limits. We illustrate that distinction between the "quasi-ballistic", and "quasi-hydrodynamic" regimes is challenging and often needs to be quantitative in nature. From first-principles calculations, we populate the resulting transport regime plots, and demonstrate how the Fermi surface orientation adds complexity to the observed transport signatures in micro-scale devices. Our work provides key insights into microscopic interaction mechanisms on open hexagonal Fermi surfaces and establishes their connection to the macroscopic electron transport in finite-size channels.

I. INTRODUCTION

Signatures of unconventional transport in condensed matter systems have been the subject of active research in fields ranging from materials physics to computational hydrodynamics and statistical physics. Despite the success of the Drude theory in describing the dynamics of charge transport in bulk metals and semimetals at and near the Fermi level [1], finite-size effects and the interplay between the geometrical and topological character of the Fermi surface can give rise to unconventional transport regimes. Of particular interest, is the electron 'hydrodynamic' transport regime, which manifests itself in negative non-local resistance and non-uniform current distributions [2–4], when the momentum-relaxing collisions of electrons with impurities, phonons, and the boundary are significantly slower than the momentum-conserving electron-electron collisions. Experimental evidence and observations of hydrodynamic flow in condensed matter systems has been steadily increasing in recent years across a handful of systems, such as two dimensional electron gases (2DEG) (Al,Ga)As [3], graphene [5–9], and some bulk (semi)metals with nontrivial electronic structures [10–14].

Among these systems, layered delafossites, such as PdCoO$_2$ and PtCoO$_2$ (Figure 1a), are highly conductive metals with open hexagonal Fermi surfaces (Figure 1b), which can host long electron mean free paths even at the room temperature [15, 16], making them ideal candidates to observe finite-size effects in electron transport. Despite their simple electronic structure, many interesting transport signatures have been observed in these systems, including large magnetoresistance and deviations from KohlerâĂŹs relation at finite

temperatures [12, 17], super-geometric electron focusing [18], commensurability oscillations [19], upturn of in-plane resistivity [16], directional ballistic effects [20], deviation between optical and transport scattering rate measurements at low temperatures [21], and phonon drag effect in thermopower measurements [22]. Curiously, the thermopower of PdCoO$_2$ was predicted to have the opposite signs along the in-plane and out-of-plane directions [15, 23]. Such axis-dependent $p-$ and $n-$type conduction has recently been proposed to originate from the open concave Fermi surface shape [24–26]. The emergence of such rich transport phenomena from a relatively simple electronic structure, poses many open questions. For example, the extremely long carrier mean free path at low temperatures [16, 27], combined with the recent observation of directional ballistics [20], has rekindled discussions on the hydrodynamic-character of electron transport in delafossite metals [13, 20, 28].

In this *Article*, we address these unconventional electron transport phenomena from a two dimensional Fermiology perspective, using PdCoO$_2$ as a model system. We establish the microscopic origins of electron scattering, from first principles, including momentum-relaxing events (electron-phonon and electron-impurity scattering) and momentum-conserving events (electron-electron scattering through the direct Coulomb interaction and exchnage of a virtual phonon). We present these temperature-dependent electron mean free paths and discuss the dominant phonon dynamics arising from phonon-phonon and phonon-electron interactions. We find that the phonon-mediated electron-electron interactions dominate the momentum-relaxing mechanisms at a wide temperature range, opening up the possibility for observing hydrodynamic electron transport regime. Further, we explicitly examine the effects of Fermi surface anisotropy in the Boltzmann transport equation (BTE), which we use to extract the electron current flows in different transport *limits*. Using the microscopic length scales from the first principle calculations, we eluci-

---
[*] These authors contributed equally.
[†] Electronic address: prineha@seas.harvard.edu

date how the electron scattering physics manifest in unconventional transport phenomena in micro-scale samples. Building on this, we plot the current profile curvature and in-plane conductivity for a range of momentum-relaxing and momentum-conserving interactions, allowing for classification of different transport regimes. This work establishes a theoretical framework to understand electron transport in PdCoO$_2$ by providing first-principles insights into microscopic electron scattering mechanisms and bridging them with the Fermi surface geometry. The approach demonstrated here is applicable to other condensed matter systems, including Dirac/Weyl semimetals, in predicting the emergence of hydrodynamics in these systems and distinguishing it from other transport regimes.

II. RESULTS AND DISCUSSION

A. Anisotropic BTE and electron transport limits

The evolution of a non-equilibrium charge carrier distribution function at steady-state and in the presence of an external electric field $\boldsymbol{E}$ is given by the semi-classical BTE:

$$\boldsymbol{v}_s \cdot \nabla_{\boldsymbol{r}} f(s, \boldsymbol{r}) + q\boldsymbol{E} \cdot \nabla_s f(s, \boldsymbol{r}) = \Gamma_s[f], \quad (1)$$

where $f(s, \boldsymbol{r})$ is the non-equilibrium charge carrier distribution function around position $\boldsymbol{r}$ with state label s (encapsulating the wavevector $\boldsymbol{k}$ and band index n), $\boldsymbol{v}_s$ is the carrier's group velocity, and $\Gamma_s[f]$ is the collision-integral functional. We consider a two-dimensional infinite channel of width W, $\boldsymbol{r} = (x, y)$, and parametrize the single-band, $n = 1$, in-plane wavevector at the Fermi surface using $\boldsymbol{k} = k_F \rho(\theta) \begin{Bmatrix} \cos(\theta) \\ \sin(\theta) \end{Bmatrix}$, where k_F is the average Fermi wavevector and $\rho(\theta)$ is a polar equation defined between $\theta = 0$ and $\theta = 2\pi$, with an average value of 1. Since the drift velocity along the channel's transverse direction must vanish at steady-state (see Supplemental Material [29]), we linearize Equation (1) by introducing the parametrization

$$f(s, \boldsymbol{r}) = f(\theta, y) = qE_x v_x(\theta) l_{\text{eff}}(\theta, y), \quad (2)$$

where l_{eff} is an effective distance a charge carrier at y with momentum in the direction of θ has traveled since its last collision. Under the relaxation time approximation, this leads to the integro-differential equation [3, 11]:

$$v_y(\theta)\, \partial_y\, l_{\text{eff}}(\theta, y) + \frac{l_{\text{eff}}(\theta, y)}{l}$$
$$= 1 + \frac{1}{l_{\text{mc}}} \int_0^{2\pi} \frac{d\phi}{\pi} v_x^2(\phi) l_{\text{eff}}(\phi, y), \quad (3)$$

where l_{mc} is a momentum-conserving mean-free path, and we've used Mathiessen's rule $l^{-1} = l_{\text{mr}}^{-1} + l_{\text{mc}}^{-1}$ to combine l_{mc} with the momentum-relaxing mean free path l_{mr}. The Fermi-surface anisotropy is introduced through the Fermi velocity term

$$\boldsymbol{v} = v_F \begin{Bmatrix} \cos(\theta)\rho(\theta) + \sin(\theta)\rho'(\theta) \\ \sin(\theta)\rho(\theta) - \cos(\theta)\rho'(\theta) \end{Bmatrix}. \quad (4)$$

The in-plane Fermi surface of PdCoO$_2$, based on Angle-resolved photoemission spectroscopy (ARPES) measurements [20], is shown in Figure 1c. While the hexagonal Fermi surface does not deviate strongly from an isotropic (circular) Fermi surface, its faceted nature leads to a highly anisotropic velocity distribution (Figure 1c).

Before examining the effects of this velocity anisotropy on Equation (3), it is instructive to clarify *limits* arising in electron transport regimes, namely the common diffusive or "Ohmic" regime and the more exotic hydrodynamic or "Poiseuille" limit. These limits arise in wide-enough channels when one of the momentum-relaxing or momentum-conserving collisions dominate over the other and result in completely uniform or completely parabolic current profiles for "Ohmic" (Figure 1d-f black) and "Poiseuille" (Figure 1d-f blue) flows respectively. In finite-size conductors, these scattering length scales additionally compete with the channel's boundary, giving rise to ballistic transport, where the scattering with the sample wall is the dominating mechanism.

Given that in high quality crystals momentum-relaxing mean free paths are on the order of microns, electron transport regimes in micro- and nanoscale devices exist somewhere on a spectrum between the "Ohmic", "Poiseuille", and ballistic limits. The macroscopic observables are closely related to the hierarchy of the microscopic length scales in a system. Further, realistically electronic transport in materials happens in presence of all scattering events, therefore we term "quasi-diffusive" ($l_{mr} \ll W \ll l_{mc}$), "quasi-ballistic" ($W \ll l_{mr} \ll l_{mc}$), and "quasi-hydrodynamic" ($l_{mc} \ll W \ll l_{mr}$) to further highlight the continuous transition between these limiting regimes. The expected current profiles under each *limit* and in these three regimes are shown in Figure 1d-f. It is worth emphasizing that, given that the quasi-hydrodynamic regime arises mostly from momentum-conserving scattering events, which cannot be readily captured using traditional transport measurements such as resistivity, experimentally detecting the manifestation of such current profiles is not trivial. Despite recent work in probing hydrodynamic signatures using optical conductivity measurements [30], and microwave induced resistance oscillation [31] in graphene and 2DEGs, quantifying hydrodynamic effects from bulk transport measurements remains very challenging in high carrier density metals and semimetals. [32, 33] This is in-part due to the continuous transition of the various transport regimes, as-well as the finite-size effects introduced by the sample geometry. Another layer of complexity arises from the fact that in the hydrodynamic regime, the momentum-conserving mean free path (l_{mc}) is not homogeneously related to the resistivity [3, 34], but rather one needs to solve for the spatially-resolved current density distribution, whose integration gives an effective bulk resistivity [3].

Recently, spatially resolved measurements have revealed non-uniform current density distributions in graphene [8, 9, 35] and WTe$_2$ [11] conducting channels. These techniques have distinct advantages in diagnosing the hydrodynamic signatures that are difficult to pinpoint without careful and integrated examination of bulk transport measurements. [32] As such, we use the calculated current density distribution, and specifically its curvature in the middle of the channel, as an
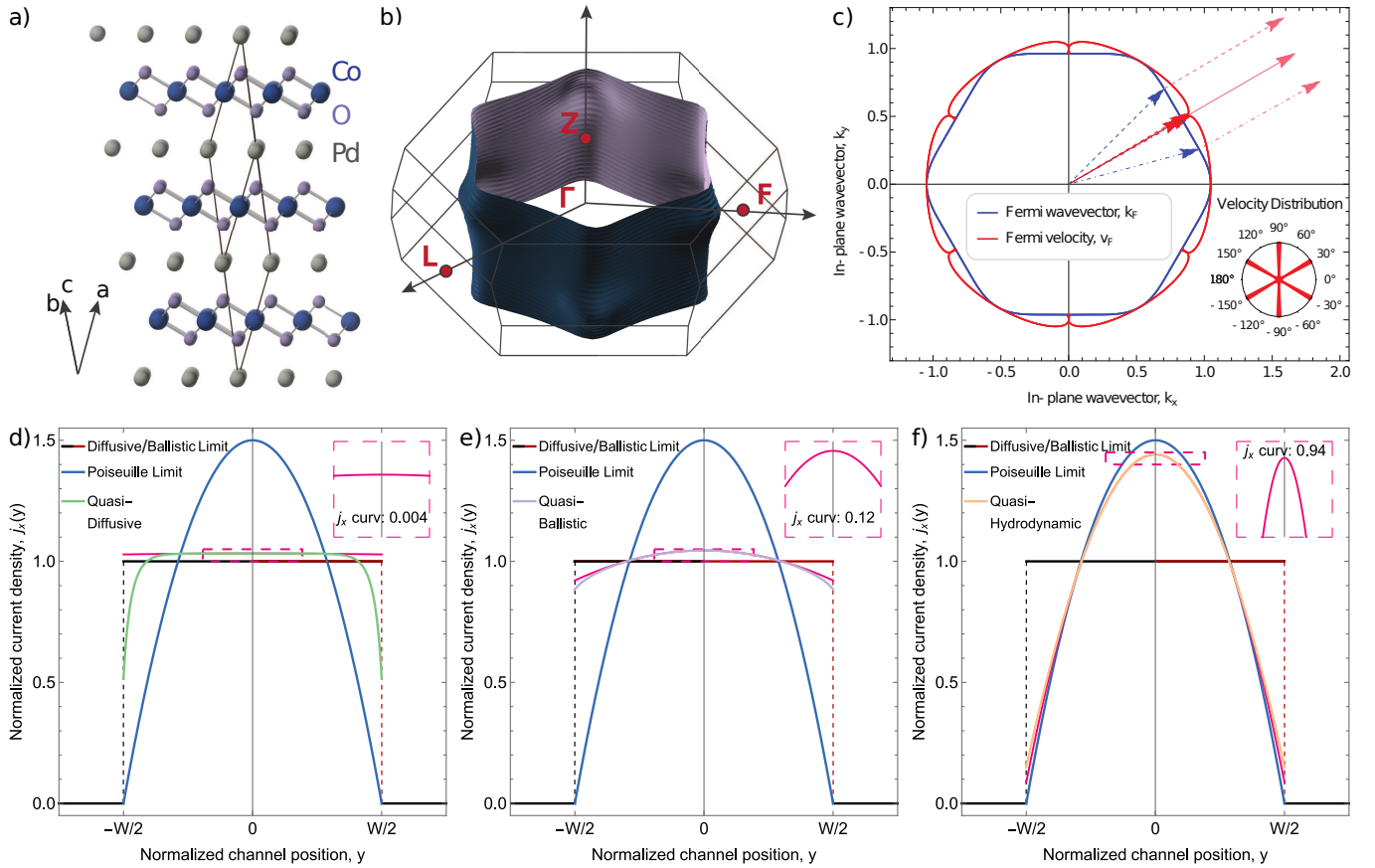
Figure 1. **(a)** Rhombohedral lattice structure of PdCoO$_2$ highlighting the vdW layers. **(b)** Fermi surface of PdCoO$_2$ in the first Brillouin zone, with the high symmetry points denoted by red markers, showing an open faceted-cylindrical shape along the out-of-plane ($\Gamma - Z$) direction. **(c)** Polar plot of Fermi wavevector from ARPES measurements for PdCoO$_2$ (blue). Blue arrows plot the Fermi wavevector at $15°$, $30°$, and $45°$. Pink arrows plot the vector perpendicular to the Fermi surface at those orientations, i.e. the Fermi velocity. Translated back to the zone origin, and plotted over all angles, red polar plot shows the angular dependence of the Fermi velocity. Note the nearly flat Fermi surface facets lead to a notable anisotropy in the velocity distribution (inset sector chart). Area-normalized current density profiles in a channel of width W for **(d)** "quasi-diffusive", **(e)** "quasi-ballistic", and **(f)** "quasi-hydrodynamic" regimes. **(d-f)** also plot the fully-diffusive (black) and fully-parabolic (blue) limits for reference. Insets plot the best fit parabola at the middle of the channel, from which normalized current density curvatures are extracted.

important metric to discuss transport phenomena in finite-size PdCoO$_2$. Finally, we note that hydrodynamic effects are significant when the hierarchy of the electron length scales due to scattering events, including momentum-relaxing scattering with phonons and impurities (l_{mr}), momentum-conserving scattering with other electrons (l_{mc}), as well as scattering with the boundary of the channel (W) satisfies the inequalities $l_{mc} \ll W \ll l_{mr}$ [28, 36]. This naturally leads to the observation that ballistic and hydrodynamic effects can coexist and contribute to the overall transport measurements.

B. Microscopic scattering mechanisms in PdCoO$_2$

As previously discussed, it is challenging to distinguish transport signatures between the quasi-hydrodynamic and quasi-ballistic regimes. Consequently, it is important to address the microscopic mechanisms giving rise to each regime using first-principle calculations of electron lifetimes due to

scattering events specific to the materials in question. For instance, in WTe$_2$ phonon-mediated momentum-conserving electron interactions dominate momentum-relaxing interactions of electrons with phonons and impurities at intermediate temperatures and thus lead to hydrodynamic transport flow [11]. This scattering mechanism is often overlooked in studies of low-carrier density materials, where electrons scatter predominantly through the more-direct Coulomb interaction. By contrast, bulk PdCoO$_2$ has a highly dispersive band with considerable carrier concentration at the Fermi level, where the Coulomb interaction is expected to be screened contributing weakly to electron-electron scattering.

Figure 2a plots the temperature dependent electron mean free paths computed for various interactions using first principles. Here, momentum relaxing (l_{mr}) events include the electron-phonon scattering (l_{eph}), which decreases rapidly with increasing temperature and the electron-impurity scattering (l_{imp}), which is largely temperature independent and dominated by the impurity concentration in the sample. Momentum
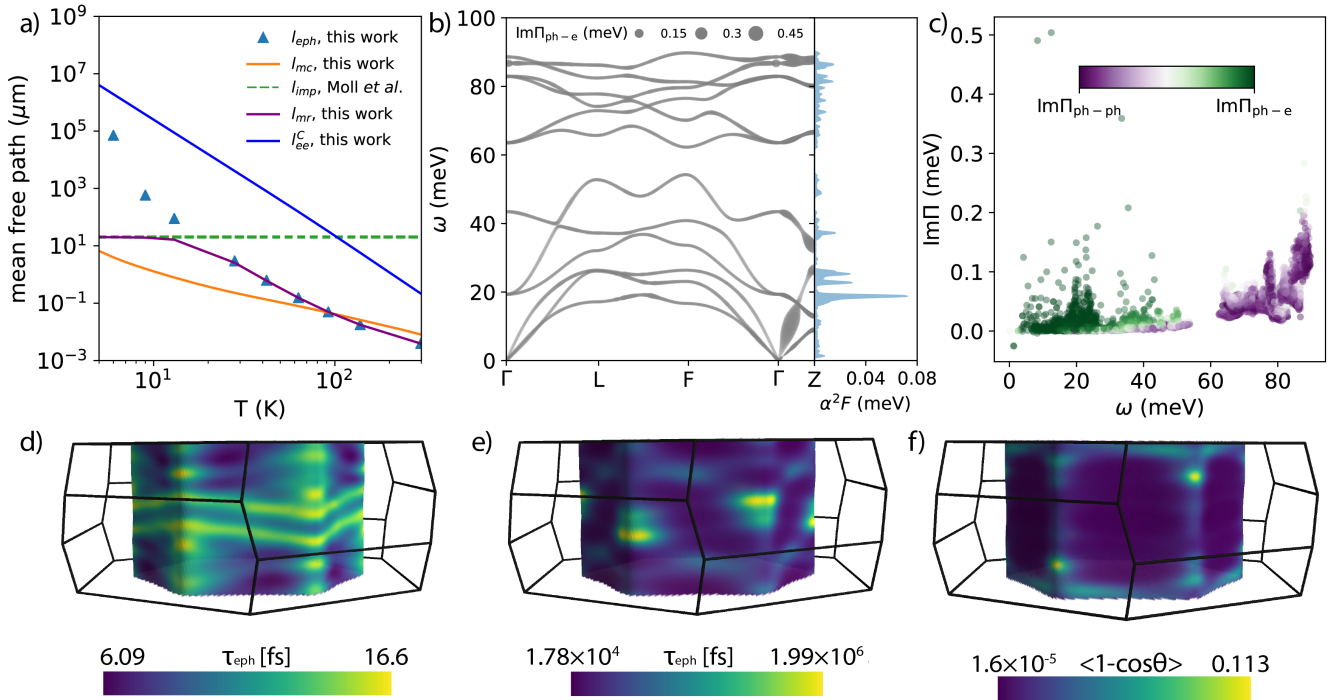
Figure 2. **(a)** Temperature dependent electron mean free pahts for PdCoO$_2$, obtained from *ab initio* calculations (see Methods). We consider electron-phonon (l_{eph}), electron-impurity (l_{imp}), electron-electron scattering mediated by a screened Coulomb interaction (l_{ee}^C), and by a virtual phonon (l_{mc}). The momentum relaxing mean free path, l_{mr}, is computed using Matthiessen's rule. **(b)** Phonon dispersion of PdCoO$_2$ along the high symmetry path in the Brillouin zone (Figure 1b), with the marker size indicating the imaginary part of phonon-electron self energy (ImΠ_{ph-e}) calculated at 25 K. The corresponding Eliashberg coupling function for different phonon frequencies, $\alpha^2F(\omega)$ (see Methods), is plotted in the right panel. **(c)** Comparison of phonon self energies at 25 K resulting from phonon-phonon (ImΠ_{ph-ph}) and phonon-electron coupling (ImΠ_{ph-e}), highlighting that the phonon-electron interaction dominates the low energy modes at low temperatures. Anisotropic scattering distribution on the Fermi surface, illustrating $\tau_{eph}(n\mathbf{k})$ at **(d)** 300 K, **(e)** 4 K, and **(f)** the scattering efficiency $<1-\cos\theta>$ at 4 K.

conserving events (l_{mc}) include the electron-electron scattering mediated by the direct Coulomb interaction (l_{ee}^C), as well as by a virtual phonon. The temperature dependence of the direct Coulomb interaction is well-known within Fermi-liquid theory to be T^2. Here, we calculate the computationally-intensive electron-electron linewidths at room-temperature, and use an analytical expression to extend the results to lower temperatures (for details see Sec. IV D). The phonon-mediated electron mean free path should in principle also exhibit a T^2 dependence at the low-temperature limit [37, 38]. We note however that at the lowest temperature we computed for PdCoO$_2$ (6 K), this effect has not yet overtaken the high-temperature limit. For the momentum-relaxing events, below ~ 10 K, the long electron-phonon mean free path in PdCoO$_2$ leaves the resistivity fully determined by the impurity length. Particularly, the as-grown samples are shown to be resistant to defect formation [27], and the resulting long l_{mr} provides a temperature-window for l_{mc} to dominate the dynamics. Similar to observations in WP$_2$ [38] and WTe$_2$ [11], the Coulomb-mediated electron-electron mean free paths are orders of magnitude longer than those associated with the other mechanisms, due to their high carrier density. Importantly, the phonon-mediated mean free paths in PdCoO$_2$ start to play an important role at ~ 100 K, and significantly dominate over l_{mr} below 30 K, indicating the possibility

for quasi-hydrodynamic flow when the channel width satisfies $l_{mc} \ll W \ll l_{mr}$.

To understand the role of phonons in the electronic transport through this phonon mediated interaction, we investigate the phonon dynamics by comparing the phonon self-energies due to phonon-electron and phonon-phonon interactions. Figure 2b plots the imaginary part of the phonon self-energy (ImΠ_{ph-e}) due to phonon-electron interactions for different phonon modes (left panel). The phonon dispersion is calculated along the high-symmetry lines in the Brillouin zone illustrated in Fig. 1b, where Γ-F and Γ-L represent the in-plane direction while Γ-Z represents the cross-plane direction along the stacking of the [CoO$_2$]$^{-1}$ layers. The cross-plane phonon modes show much larger self-energies than the in-plane ones, for both acoustic and optical branches, indicating these modes are more strongly coupled with electrons. The Eliashberg spectral function, plotted at different phonon frequencies (Fig. 2b: right panel), indicates that the lower energy optical phonon modes contribute the most.

Further, since the phonon-mediated electron electron interaction proceeds via the exchange of a 'virtual' phonon, i.e. the phonon emitted (absorbed) by a pair of electrons is assumed to by 'instantaneously' absorbed (emitted) by a different pair of electrons, we explicitly examine the phonon self-energies due

to the competing phonon-phonon interactions ($\mathrm{Im}\Pi_{\mathrm{ph-ph}}$) to justify this assumption. Fig. 2c compares the two phonon scattering mechanisms at 25 K, well within the temperature window identified in Fig. 2a for manifesting quasi-hydrodynamic flow. While the high energy optical modes feature stronger phonon-phonon scattering, the lower energy ones show much stronger phonon-electron interactions. As such, at low temperatures where only lower-energy phonon modes are occupied, the phonon linewidths follow $\mathrm{Im}\Pi_{\mathrm{ph-ph}} \ll \mathrm{Im}\Pi_{\mathrm{ph-e}}$, indicating that phonons rapidly exchange their momentum with electrons instead of relaxing their momentum to the lattice, i.e. thermalizing. As the lattice temperature increases, phonon-phonon interactions increase and finally overtake the phonon-electron coupling (see Supplemental Material [29]). Recently, the unconventional temperature-dependent phonon linewidth decay observed in a Raman study in WP_2 [39], was also attributed to the strong phonon-electron coupling leading to the similar hierarchy of the quasiparticle lifetimes.

In the absence of electron-impurity scattering, $PdCoO_2$ exhibits extremely long electron-phonon scattering mean free paths (Figure 2a blue markers). To better understand the origin of these long-lived electrons, we computed the state-resolved electron-phonon lifetimes (τ_{eph}) for the single energy band. For transport properties, only the states (with energy $\varepsilon_{\vec{k}}$) near the Fermi level matter, typically weighted by $-f'(\varepsilon_{\vec{k}})$ in the Boltzmann relaxation time approximation (RTA). The distribution of the strongly anisotropic τ_{eph} on the hexagonal Fermi surface is displayed in Figure 2d-e for high (300 K) and low (4 K) temperatures, with yellow color corresponding to "long-lived" carriers. While at higher temperatures, the long τ_{eph} is more-evenly distributed between the faces and the edges of the hexagonal Fermi surface, the low temperature calculations show a much sharper contrast, whereby "long-lived" carriers are only present in regions of the Fermi surface with large Gaussian curvature. Further, while the difference between "long-" and "short-lived" carriers is within a factor of three at 300 K, it spans more than two orders of magnitude at 4 K. Further, we augment the scattering rate with an efficiency factor given by the relative change in direction of the initial and final state velocities $\left(1 - \frac{v_{n\mathbf{k}} \cdot v_{m\mathbf{k}'}}{|v_{n\mathbf{k}}||v_{m\mathbf{k}'}|}\right| = 1 - \cos(\theta)\right)$ [40], where θ is the scattering angle between the initial and final electronic states. Phonon modes strongly coupled with electrons appear to have a small momentum transfer $\mathbf{q}$ at very low temperatures, resulting in the vanishing scattering efficiency, shown by $< 1 - \cos\theta > \approx 0$ in Figure 2f. Further, "long-lived" carriers at low temperatures correlate with regions of larger negative Gaussian curvature(Figure 1). This can give rise to rich transport phenomena in $PdCoO_2$ micron-scale devices as we discuss in greater detail below, as the momentum relaxing electron mean free path can reach $\sim 20\mu m$ at low temperatures even in the presence of impurities [13, 20].

C. Electron transport regimes

Equipped with the temperature-dependent momentum-relaxing and momentum-conserving mean free paths for $PdCoO_2$ using first-principles, we solve Equation (3) for a range of (l_{mr}/W, l_{mc}/W) pairs to examine the dominating transport regimes at different temperatures. Figure 3a shows a contour plot of the curvature of the current profile at the middle of the channel for a hexagonal Fermi surface aligned at $0°$ with the channel, with the "quasi-diffusive", "quasi-ballistic", and "quasi-hydrodynamic" regimes corresponding to the bottom right ($l_{\mathrm{mc}} \gg W, l_{\mathrm{mr}} \ll W$), top right ($l_{\mathrm{mc}}, l_{\mathrm{mr}} \gg W$), and top left ($l_{\mathrm{mr}} \gg W, l_{\mathrm{mc}} \ll W$) respectively. The overlaid green points mark the *ab initio* temperature trajectory Figure 2a, with lighter color indicating lower temperature. Due to the large ratio of l_{mr} to l_{mc}, the phonon-mediated electron interactions lead to a strongly non-uniform profile between 10-25K. At these temperatures, the length scales in $PdCoO_2$ reach the condition of $l_{mr} \sim 3W \sim 10l_{mc}$, where we expect $PdCoO_2$ to exhibit the strongest hydrodynamic effect. In practice, this regime can be realized in a single-crystal conducting channel a few microns wide, which has been experimentally accessible in previous work [11, 13]. In addition, there a few major indications of the physics in this regime. First, the material has very low defect level that the scattering length with impurities l_{imp} is at the scale of microns. Second, the electrons are exchanging momentum rather rapidly with the lattice, however at a cryogenic temperature, the phonons do not have spontaneous momentum transfer thus electrons obtain the momentum back and the total electron momentum is quasi-conserved. To address the anisotropy of the hexagonal Fermi surface shape, we compare the same calculation for a rotated Fermi surface aligned at $30°$ with the channel, shown in Figure 3b. We observe a considerable decrease in the observed current profile curvature, indicating a transition away from quasi-hydrodynamic to quasi-ballistic behavior. Intuitively, this directional dependence peaks in the "quasi-ballistic" regime as the boundary scattering dominates, and vanishes in the "quasi-diffusive" limit as the multiple scattering events serve to effectively randomize the carriers' velocity directions. This can also be intuitively seen from the fact that the highly directional dependent distribution of the Fermi velocity v_F (fig. 1c) is the main reason of the unexpected directional dependence in electron transport. If $W \ll l_{mr} = v_F\tau_{mr}$, even the direction featuring the smallest v_F satisfies the ballistic limit $v_F \gg W/\tau_{mr}$, there will be hardly any difference even if the greater v_F is taken into account. Similarly, in the "quasi-diffusive" limit, the electrons will never reach the boundary of the channel, thus the transport observables comes from the Fermi surface integral of all electron velocities.

Moreover, such directional dependence of the current flow is strongly manifested in the device's in-plane conductivity (Figure 3c), which is directly observable from transport measurements. This anisotropic effect is strongest in the absence of momentum-conserving interactions (i.e. at the far-right of Figure 3), indicating the emergence of 'easy' and 'hard' transport directions [20]. As momentum-conserving interactions lead to collective flow which likewise acts to homogenize the carriers' velocity directions, the effect gets weaker in the quasi-hydrodynamic regime identified between 10-25 K, albeit still expected to be measurable. Figure 3d plots the % increase for both current density curvatures (top) and the in-plane conduc-
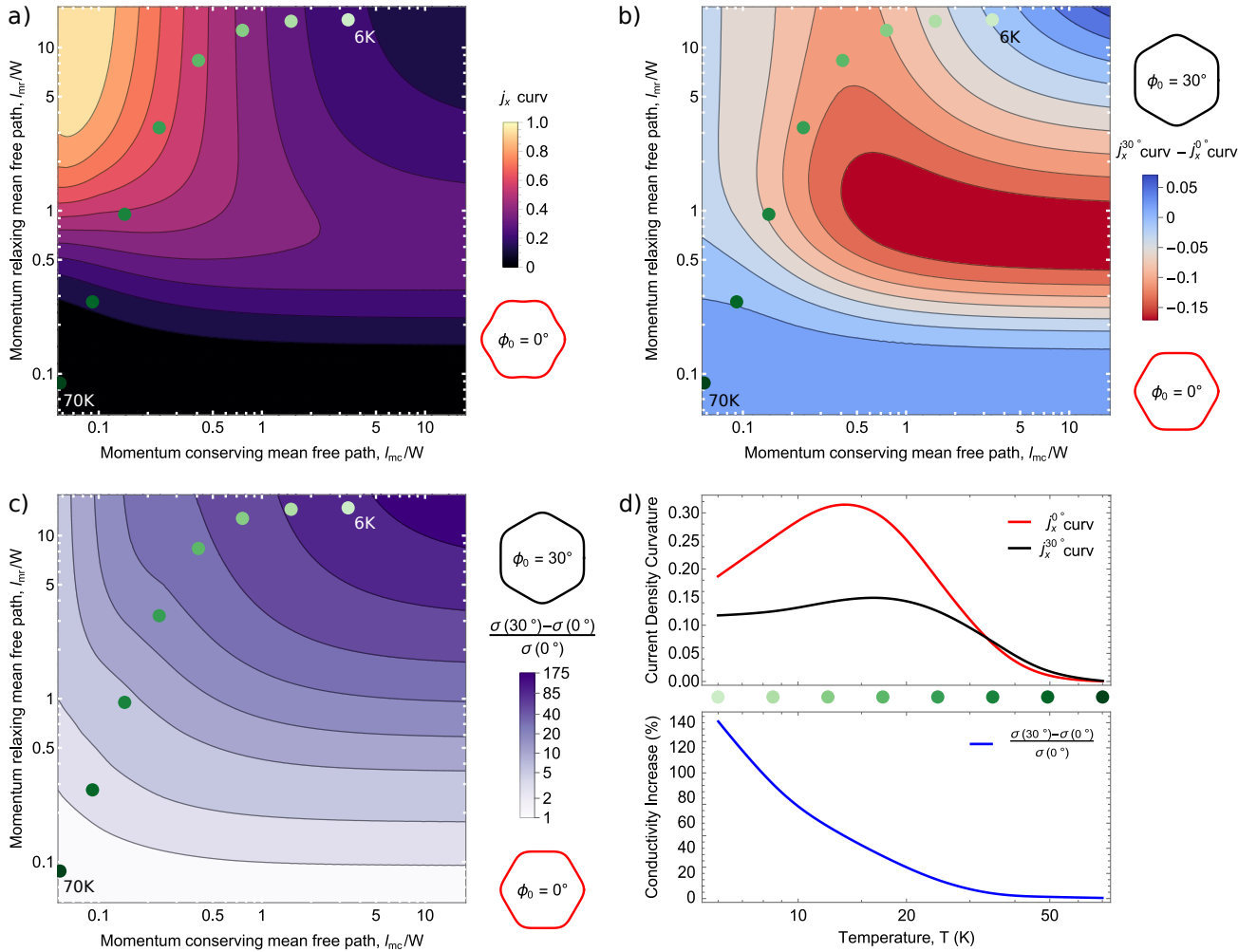
Figure 3. **(a)** Current density curvature contour plot over a large range of momentum-conserving (l_{mc}/W, x-axis) and momentum-relaxing (l_{mr}/W, y-axis) interactions, for a system with Fermi surface shown in red in the inset. Overlaid points plot the *ab initio* temperature-dependent mean free paths for a 1.25 μm wide channel of PdCoO$_2$ with an impurity level of 18.5 μm; temperature range is 6K (lightest green) to 70K (darkest green). **(b)** Current density curvature difference between the system shown in (a) and the same with a rotated Fermi surface at $30°$ with respect to the channel (black inset). The decrease in curvature is indicative of the shift from "quasi-hydrodynamic" to "quasi-ballistic" flow. **(c)** Percent difference in in-plane conductivity between the two Fermi surface orientations showin in (b). **(d)** Current density curvature (top) and percent difference in conductivity (bottom) along the *ab initio* temperature trajectory shown by the overlaid green points in (a-c). While the directional dependence naturally manifests itself most prominently in the "quasi-ballistic" regime, it is still evident in the "quasi-hydronamic" window between 10-25K.

tivity (bottom) as a function of temperature, the latter of which has been recently observed in Ref. [18, 20]. These transport regime plots effectively bridge together the microscopic scattering events and the exotic transport signatures in PdCoO$_2$ and highlight how the Fermi surface topology could give rise to behaviors deviating from the simple kinetic picture.

III. CONCLUSIONS

We present an investigation of unconventional electron transport in the delafossite metal PdCoO$_2$, using a combination of first-principles methods and numerical modeling of the anisotropic BTE. We examine the temperature-dependent electron mean free paths, with an emphasis on establishing the hierarchy of the momentum-relaxing (l_{mr}) and momentum-conserving (l_{mc}) interactions. We show that while the direct Coulomb interaction is largely screened due to the metal's high carrier density, the phonon-mediated electron-electron interaction dominates momentum-relaxing electron interactions in the temperature range of $4-100$ K. This mechanism is supported by the much smaller phonon-phonon self-energies compared to the phonon-electron interaction at low temperatures. We develop the formalism for an anisotropic BTE which treats the ARPES-measured in-plane Fermi surface shape, and obtain the numerical solutions for a wide range of l_{mr}/W,

l_{mc}/W pairs. We discuss the resulting transport regime *limits* and demonstrate the directional dependence of these transport measurements with regards to the orientation of the Fermi surface to the conducting channel.

Our work offers insight into previous observations of in $PdCoO_2$, and presents a comprehensive theoretical framework to distinguish the quasi-ballistic and quasi-hydrodynamic transport regimes. The strong phonon-mediated electron interactions suggest the possibility of hydrodynamics in $PdCoO_2$, which we anticipate will spark experimental investigation via spatially resolved techniques. Finally, our findings serve as a foundation for understanding electron transport from microscopic scattering mechanisms and Fermi surface geometry, and motivate future efforts in computing the electronic viscosity in such material systems directly from first principles.

IV. METHODS

A. Computational Details

The *ab initio* calculations were performed with the open source density functional theory (DFT) code JDFTx [41]. The structure of $PdCoO_2$ was fully relaxed using Perdew-Burke-Ernzerhof norm-conserving pseudopotentials [42]. A kinetic cutoff energy of 50 Ha was used along with a $6\times6\times6$ Gamma-centered k-mesh, and a Fermi-Dirac smearing of 0.01 Ha for the Brillouin zone integration. Both the lattice constants and the ion positions were relaxed until the forces on all atoms were less than 10^{-8} Ha/Bohr. The relaxed lattice parameters were found to be $a = b = c = 6.1$ Å, $\alpha = \beta = \gamma = 26.65°$, respectively. To compute the e-ph scattering time, we performed frozen phonon calculations in a $3\times3\times3$ supercell, and obtained 18 maximally localized Wannier functions (MLWFs) by projecting the plane-wave bandstructure to Pd-*s,d*, Co-*s,d* and O-*p* orbitals [43, 44]. We then collected the electron scattering rates on a much finer $36\times36\times36$ **k** and **q** grid for convergence. For the screened Coulomb mediated electron-electron scattering, a dielectric matrix cutoff of 120 eV was used to include enough empty states, with a energy resolution of 0.01 eV. The phonon dispersion was calculated using the *ab initio* package QUANTUM ESPRESSO [45, 46] within functional perturbation theory, using the PBE exchange-correlation functional [47, 48]. Further, we computed electron-phonon coupling matrix elements and phonon-electron linewidths $ImΠ_{ph−e}$ with the EPW package [49], by interpolating the maximally localized Wannier functions on an initial coarse $6 \times 6 \times 6$ **k** and $3 \times 3 \times 3$ **q** grids, from which we computed the phonon self-energies on a finer $60 \times 60 \times 60$ **k** grids. The phononâĂŞphonon scattering process in our theoretical calculations has been performed on a $2\times2\times2$ supercell using the *phono3py* package [50] to calculate the second-order (harmonic) and third-order (an-harmonic) interatomic force constant matrices. A uniform $15 \times 15 \times 15$ **q**-grid was adopted for the final calculation of the phonon self energies $ImΠ_{ph−ph}$.

B. Electron-phonon scattering

We obtain the electron-phonon scattering time (τ_{eph}) from the electron self energy by Fermi's golden rule following:

$$\tau_{eph}^{-1}(n\mathbf{k}) = \frac{2\pi}{\hbar} \sum_{m\nu} \int_{BZ} \frac{d\mathbf{q}}{\Omega_{BZ}} \left|g_{mn,\nu}(\mathbf{k},\mathbf{q})\right|^2$$
$$\times [(n_{\mathbf{q}\nu} + \frac{1}{2} \mp \frac{1}{2})\delta(\varepsilon_{n\mathbf{k}} \mp \omega_{\mathbf{k}\nu} - \varepsilon_{m\mathbf{k+q}})], \quad (5)$$

where Ω_{BZ} is the Brillouin zone volume, $f_{n\mathbf{k}}$ and $n_{\mathbf{q}\nu}$ are the Fermi-Dirac and Bose-Einstein distribution functions, respectively. The incident electron with energy $\varepsilon_{n\mathbf{k}}$ (n for band index and **k** for the wavevector) is scattered by a phonon of frequency $\omega_{\mathbf{q}\nu}$ (with **q** the momentum and ν the branch index), resulting in the scattered electron state $\mathbf{k} + \mathbf{q}$ with m the new band index. The e-ph matrix element for such scattering vertex is given by

$$g_{mn,\nu}(\mathbf{k},\mathbf{q}) = \left(\frac{\hbar}{2m_0\omega_{\mathbf{q}\nu}}\right)^{1/2} \langle\psi_{m\mathbf{k+q}}|\partial_{\mathbf{q}\nu}V|\psi_{n\mathbf{k}}\rangle, \quad (6)$$

where $\langle\psi_{m\mathbf{k+q}}|$ and $|\psi_{n\mathbf{k}}\rangle$ denote the Bloch eigenstates and $\partial_{\mathbf{q}\nu}V$ is the perturbation of the self-consistent potential with respect to ion displacement associated with a phonon branch with frequency $\omega_{\mathbf{q}\nu}$. The momentum-relaxing electron scattering rates are evaluated by accounting for the change in momentum between final and initial states based on their relative scattering angle (referred to as "scattering efficiency" in the main text) following

$$\left(\tau_{eph}^{mr}(n\mathbf{k})\right)^{-1} = \frac{2\pi}{\hbar} \sum_{m\nu} \int_{BZ} \frac{d\mathbf{q}}{\Omega_{BZ}} \left|g_{mn,\nu}(\mathbf{k},\mathbf{q})\right|^2$$
$$\times [(n_{\mathbf{q}\nu} + \frac{1}{2} \mp \frac{1}{2})\delta(\varepsilon_{n\mathbf{k}} \mp \omega_{\mathbf{q}\nu} - \varepsilon_{m\mathbf{k+q}})]$$
$$\times \left(1 - \frac{v_{n\mathbf{k}} \cdot v_{n\mathbf{k}}}{|v_{n\mathbf{k}}||v_{n\mathbf{k}}|}\right), \quad (7)$$

where $v_{n\mathbf{k}}$ is the group velocity. To account for the temperature dependence of the momentum relaxing τ_{mr}, we compute the Brillouin zone integral by taking a Fermi-surface average weighted by $|v_{n\mathbf{k}}|^2$ and the energy derivative of the Fermi occupation for transport properties following

$$\tau_{eph}^{mr} = \frac{\int_{BZ} \frac{d\mathbf{k}}{(2\pi)^3} \sum_n \frac{\partial f_{n\mathbf{k}}}{\partial \varepsilon_{n\mathbf{k}}} |v_{n\mathbf{k}}|^2 \tau_{eph}^{mr}(n\mathbf{k})}{\int_{BZ} \frac{d\mathbf{k}}{(2\pi)^3} \sum_n \frac{\partial f_{n\mathbf{k}}}{\partial \varepsilon_{n\mathbf{k}}} |v_{n\mathbf{k}}|^2}. \quad (8)$$

C. Phonon mediated electron-electron scattering

The electron-electron scattering rate mediated by a virtual phonon can be estimated within the random phase approximation by

$$(\tau_{ee}^{PH})^{-1} = \frac{\pi\hbar^2}{2k_BTg(\varepsilon_F)} \sum_\nu \int \frac{\Omega_{BZ}d\mathbf{q}}{(2\pi)^3} G_{\mathbf{q}\nu}^2$$
$$\times \int_{-\infty}^{+\infty} \frac{\omega^2 d\omega}{|\bar{\omega}_{\mathbf{q}\nu} - \omega|^2 \sinh^2\frac{\hbar\omega}{2k_BT}}, \quad (9)$$

where $g(\varepsilon_F)$ is the density of states at the Fermi level, and $\bar{\omega}_{\mathbf{q}\nu} = \omega_{\mathbf{q}\nu}(1 + i\pi G_{\mathbf{q}\nu})$ is the complex phonon frequency. The phonon-electron scattering linewidth for each phonon mode is given at the Eliashberg level of theory by

$$G_{\mathbf{q}\nu} = \sum_{mn} \int \frac{\Omega_{\mathrm{BZ}}d\mathbf{k}}{(2\pi)^3} |g_{mn,\nu}(\mathbf{k},\mathbf{q})|^2$$
$$\times \delta(\varepsilon_{n\mathbf{k}} - \varepsilon_F)\delta(\varepsilon_{m\mathbf{k+q}} - \varepsilon_F). \tag{10}$$

D. Coulomb screening mediated electron-electron scattering

The electron-electron scattering rate mediated by the screened Coulomb interaction is obtained by the imaginary part of the quasiparticle self energy at each momentum and state ($\mathrm{Im}\Sigma_{n\mathbf{k}}(n\mathbf{k})$) as

$$\tau_{\mathrm{ee}}^{-1}(n\mathbf{k}) = \frac{2\pi}{\hbar} \int_{\mathrm{BZ}} \frac{d\mathbf{k}'}{(2\pi)^3} \sum_{n'} \sum_{\mathbf{GG}'} \tilde{\rho}_{n'\mathbf{k}',n\mathbf{k}}(\mathbf{G})\tilde{\rho}_{n'\mathbf{k}',n\mathbf{k}}^*(\mathbf{G}')$$
$$\times \frac{4\pi e^2}{|\mathbf{k}' - \mathbf{k} + \mathbf{G}|^2} \mathrm{Im}[\epsilon_{\mathbf{GG}'}^{-1}(\mathbf{k}' - \mathbf{k}, \varepsilon_{n,\mathbf{k}} - \varepsilon_{n'\mathbf{k}'})], \tag{11}$$

where $\tilde{\rho}_{n'\mathbf{k}',n\mathbf{k}}(\mathbf{G})$ is the plane wave expansion of the product density $\sum_\sigma u_{n'\mathbf{k}'(\mathbf{r})}^{\sigma*} u_{n\mathbf{k}}^\sigma(\mathbf{r})$ of the Bloch functions with reciprocal lattice vectors $\mathbf{G}$, and $\epsilon_{\mathbf{GG}'}^{-1}(\mathbf{k}' - \mathbf{k}, \varepsilon_{n,\mathbf{k}} - \varepsilon_{n'\mathbf{k}'})$ is the microscopic dielectric function in a plane wave basis calculated within the random phase approximation.

Since $\tau_{\mathrm{ee}}^{-1}(n\mathbf{k})$ decays quadratically from the Fermi level ε_F, we utilize the analytical relation of τ_{ee} with dependence on temperature according to the conventional Fermi-liquid theory

$$\tau_{\mathrm{ee}}^{-1}(\varepsilon, T) \approx \frac{D_e}{\hbar}[(\varepsilon - \varepsilon_F)^2 + (\pi k_B T)^2]. \tag{12}$$

We then obtain τ_{ee}^{-1} at different temperatures by fitting all the self energies in the entire Brillouin zone for all energy bands at 298 K, extracting D_e and then adding the temperature dependence [51].

Finally, using Matthiessen's rule, the overall momentum relaxing mean free path (l_{mr}) and momentum conserving mean free path (l_{mc}) are estimated by ,

$$l_{\mathrm{mr}} = \frac{v_F}{(\tau_{\mathrm{eph}}^{\mathrm{mr}})^{-1} + (\tau_{\mathrm{imp}})^{-1}}$$
$$l_{\mathrm{mc}} = \frac{v_F}{(\tau_{\mathrm{ee}}^{\mathrm{PH}})^{-1} + (\tau_{\mathrm{ee}}^{\mathrm{W}})^{-1}}, \tag{13}$$

with v_F being the Fermi surface averaged velocity and τ_{imp} the impurity scattering time that does not have temperature dependence but can vary in different samples. We take the l_{imp} value well established in Refs. [13, 20].

[1] M. Cutler and N. F. Mott, Observation of anderson localization in an electron gas, Phys. Rev. **181**, 1336 (1969).
[2] R. Gurzhi, Hydrodynamic effects in solids at low temperature, Soviet Physics Uspekhi **11**, 255 (1968).
[3] M. J. M. de Jong and L. W. Molenkamp, Hydrodynamic electron flow in high-mobility wires, Phys. Rev. B **51**, 13389 (1995).
[4] L. Levitov and G. Falkovich, Electron Viscosity, Current Vortices and Negative Nonlocal Resistance in Graphene, Nature Physics **12**, 672 (2016).
[5] D. A. Bandurin, I. Torre, R. K. Kumar, M. B. Shalom, A. Tomadin, A. Principi, G. H. Auton, E. Khestanova, K. S. Novoselov, I. V. Grigorieva, L. A. Ponomarenko, A. K. Geim, and M. Polini, Negative local resistance caused by viscous electron backflow in graphene, Science **351**, 1055 (2016).
[6] J. Crossno, J. K. Shi, K. Wang, X. Liu, A. Harzheim, A. Lucas, S. Sachdev, P. Kim, T. Taniguchi, K. Watanabe, T. A. Ohki, and K. C. Fong, Observation of the dirac fluid and the breakdown of the wiedemann-franz law in graphene, Science **351**, 1058 (2016).
[7] R. K. Kumar, D. A. Bandurin, F. M. D. Pellegrino, Y. Cao, A. Principi, H. Guo, G. H. Auton, M. B. Shalom, L. A. Ponomarenko, G. Falkovich, K. Watanabe, T. Taniguchi, I. V. Grigorieva, L. S. Levitov, M. Polini, and A. K. Geim, Superballistic flow of viscous electron fluid through graphene constrictions, Nature Physics **13**, 1182 (2017).
[8] M. J. H. Ku, T. X. Zhou, Q. Li, Y. J. Shin, J. K. Shi, C. Burch, L. E. Anderson, A. T. Pierce, Y. Xie, A. Hamo, U. Vool, H. Zhang, F. Casola, T. Taniguchi, K. Watanabe, M. M. Fogler, P. Kim, A. Yacoby, and R. L. Walsworth, Imaging viscous flow of the dirac fluid in graphene, Nature **583**, 537 (2020).
[9] J. A. Sulpizio, L. Ella, A. Rozen, J. Birkbeck, D. J. Perello, D. Dutta, M. Ben-Shalom, T. Taniguchi, K. Watanabe, T. Holder, R. Queiroz, A. Principi, A. Stern, T. Scaffidi, A. K. Geim, and S. Ilani, Visualizing poiseuille flow of hydrodynamic electrons,

Nature **576**, 75 (2019).

[10] J. Gooth, F. Menges, N. Kumar, V. Süβ, C. Shekhar, Y. Sun, U. Drechsler, R. Zierold, C. Felser, and B. Gotsmann, Thermal and electrical signatures of a hydrodynamic electron fluid in tungsten diphosphide, Nature Communications **9** (2018).

[11] U. Vool, A. Hamo, G. Varnavides, Y. Wang, T. X. Zhou, N. Kumar, Y. Dovzhenko, Z. Qiu, C. A. C. Garcia, A. T. Pierce, J. Gooth, P. Anikeeva, C. Felser, P. Narang, and A. Yacoby, Imaging phonon-mediated hydrodynamic flow in wte2, Nature Physics **17**, 1216 (2021).

[12] N. Nandi, T. Scaffidi, P. Kushwaha, S. Khim, M. E. Barber, V. Sunko, F. Mazzola, P. D. C. King, H. Rosner, P. J. W. Moll, M. König, J. E. Moore, S. Hartnoll, and A. P. Mackenzie, Unconventional magneto-transport in ultrapure $PdCoO_2$ and $PtCoO_2$, npj Quantum Materials **3** (2018).

[13] P. J. Moll, P. Kushwaha, N. Nandi, B. Schmidt, and A. P. Mackenzie, Evidence for hydrodynamic electron flow in $PdCoO_2$, Science **351**, 1061 (2016).

[14] P. Narang, C. A. Garcia, and C. Felser, The topology of electronic band structures, Nature Materials **20**, 293 (2021).

[15] R. Daou, R. Frésard, V. Eyert, S. Hébert, and A. Maignan, Unconventional aspects of electronic transport in delafossite oxides, Science and Technology of Advanced Materials **18**, 919 (2017).

[16] C. W. Hicks, A. S. Gibbs, A. P. Mackenzie, H. Takatsu, Y. Maeno, and E. A. Yelland, Quantum oscillations and high carrier mobility in the delafossite $PdCoO_2$, Phys. Rev. Lett. **109**, 116401 (2012).

[17] H. Takatsu, J. J. Ishikawa, S. Yonezawa, H. Yoshino, T. Shishidou, T. Oguchi, K. Murata, and Y. Maeno, Extremely large magnetoresistance in the nonmagnetic metal $PdCoO_2$, Phys. Rev. Lett. **111**, 056601 (2013).

[18] M. D. Bachmann, A. L. Sharpe, A. W. Barnard, C. Putzke, M. König, S. Khim, D. Goldhaber-Gordon, A. P. Mackenzie, and P. J. Moll, Super-geometric electron focusing on the hexagonal Fermi surface of $PdCoO_2$, Nature communications **10**, 1 (2019).

[19] C. Putzke, M. D. Bachmann, P. McGuinness, E. Zhakina, V. Sunko, M. Konczykowski, T. Oka, R. Moessner, A. Stern, M. König, *et al.*, h/e oscillations in interlayer transport of delafossites, Science **368**, 1234 (2020).

[20] M. D. Bachmann, A. L. Sharpe, A. W. Barnard, C. Putzke, T. Scaffidi, N. Nandi, S. Khim, M. Koenig, D. G. Gordon, A. P. Mackenzie, *et al.*, Directional ballistic transport in the two-dimensional metal $PdCoO_2$, arXiv:2103.01332 (2021).

[21] C. C. Homes, S. Khim, and A. P. Mackenzie, Perfect separation of intraband and interband excitations in $PdCoO_2$, Phys. Rev. B **99**, 195127 (2019).

[22] R. Daou, R. Frésard, S. Hébert, and A. Maignan, Large anisotropic thermal conductivity of the intrinsically two-dimensional metallic oxide $PdCoO_2$, Phys. Rev. B **91**, 041113 (2015).

[23] K. P. Ong, D. J. Singh, and P. Wu, Unusual transport and strongly anisotropic thermopower in $PtCoO_2$ and $PdCoO_2$, Phys. Rev. Lett. **104**, 176601 (2010).

[24] B. He, Y. Wang, M. Q. Arguilla, N. D. Cultrara, M. R. Scudder, J. E. Goldberger, W. Windl, and J. P. Heremans, The Fermi surface geometrical origin of axis-dependent conduction polarity in layered materials, Nature Materials **18**, 568 (2019).

[25] Y. Wang and P. Narang, Anisotropic scattering in the goniopolar metal $NaSn_2As_2$, Phys. Rev. B **102**, 125122 (2020).

[26] Y. Wang, K. G. Koster, A. M. Ochs, M. R. Scudder, J. P. Heremans, W. Windl, and J. E. Goldberger, The chemical design principles for axis-dependent conduction polarity, Journal of the American Chemical Society **142**, 2812 (2020).

[27] V. Sunko, P. H. McGuinness, C. S. Chang, E. Zhakina, S. Khim, C. E. Dreyer, M. Konczykowski, H. Borrmann, P. J. W. Moll, M. König, D. A. Muller, and A. P. Mackenzie, Controlled introduction of defects to delafossite metals by electron irradiation, Phys. Rev. X **10**, 021018 (2020).

[28] C. Q. Cook and A. Lucas, Electron hydrodynamics with a polygonal Fermi surface, Phys. Rev. B **99**, 235148 (2019).

[29] See Supplemental Material at [url] for (i) anisotropic BTE derivation and (ii) temperature-resolved phonon self energies.

[30] P. Gallagher, C.-S. Yang, T. Lyu, F. Tian, R. Kou, H. Zhang, K. Watanabe, T. Taniguchi, and F. Wang, Quantum-critical conductivity of the dirac fluid in graphene, Science **364**, 158 (2019), https://www.science.org/doi/pdf/10.1126/science.aat8687.

[31] P. Alekseev and A. Alekseeva, Microwave-induced resistance oscillations in highly viscous electron fluid, arXiv:2105.01035 (2021).

[32] A. Jaoui, B. Fauqué, C. W. Rischau, A. Subedi, C. Fu, J. Gooth, N. Kumar, V. Süß, D. L. Maslov, C. Felser, and K. Behnia, Departure from the wiedemann–franz law in wp2 driven by mismatch in t-square resistivity prefactors, npj Quantum Materials **3**, 64 (2018).

[33] K. Behnia, On the origin and the amplitude of t-square resistivity in fermi liquids, Annalen der Physik **n/a**, 2100588, https://onlinelibrary.wiley.com/doi/pdf/10.1002/andp.202100588.

[34] T. Scaffidi, N. Nandi, B. Schmidt, A. P. Mackenzie, and J. E. Moore, Hydrodynamic electron flow and hall viscosity, Phys. Rev. Lett. **118**, 226601 (2017).

[35] A. Jenkins, S. Baumann, H. Zhou, S. A. Meynell, D. Yang, K. Watanabe, T. Taniguchi, A. Lucas, A. F. Young, and A. C. B. Jayich, Imaging the breakdown of ohmic transport in graphene, arXiv:2002.05065 (2020).

[36] A. Lucas and K. C. Fong, Hydrodynamics of electrons in graphene, Journal of Physics: Condensed Matter **30**, 053001 (2018).

[37] C. A. C. Garcia, D. M. Nenno, G. Varnavides, and P. Narang, Anisotropic phonon-mediated electronic transport in chiral weyl semimetals, Phys. Rev. Materials **5**, L091202 (2021).

[38] J. Coulter, R. Sundararaman, and P. Narang, Microscopic origins of hydrodynamic transport in the type-II weyl semimetal WP2, Physical Review B **98** (2018).

[39] G. B. Osterhoudt, Y. Wang, C. A. C. Garcia, V. M. Plisson, J. Gooth, C. Felser, P. Narang, and K. S. Burch, Evidence for dominant phonon-electron scattering in weyl semimetal wp$_2$, Phys. Rev. X **11**, 011017 (2021).

[40] J. M. Ziman, *Electrons and phonons: the theory of transport phenomena in solids* (Oxford university press, 2001).

[41] R. Sundararaman, K. Letchworth-Weaver, K. A. Schwarz, D. Gunceler, Y. Ozhabes, and T. Arias, JDFTx: Software for joint density-functional theory, SoftwareX **6**, 278 (2017).

[42] M. Schlipf and F. Gygi, Optimization algorithm for the generation of ONCV pseudopotentials, Computer Physics Communications **196**, 36 (2015).

[43] N. Marzari and D. Vanderbilt, Maximally localized generalized Wannier functions for composite energy bands, Phys. Rev. B **56**, 12847 (1997).

[44] I. Souza, N. Marzari, and D. Vanderbilt, Maximally localized Wannier functions for entangled energy bands, Phys. Rev. B **65**, 035109 (2001).

[45] P. Giannozzi, S. Baroni, N. Bonini, M. Calandra, R. Car, C. Cavazzoni, D. Ceresoli, G. L. Chiarotti, M. Cococcioni, I. Dabo, *et al.*, QUANTUM ESPRESSO: a modular and open-source software project for quantum simulations of materials, Journal of Physics: Condensed Matter **21**, 395502 (19pp) (2009).

[46] P. Giannozzi, O. Andreussi, T. Brumme, O. Bunau, M. B. Nardelli, M. Calandra, R. Car, C. Cavazzoni, D. Ceresoli, M. Cococcioni, *et al.*, Advanced capabilities for materials modelling with Quantum ESPRESSO, Journal of Physics: Condensed Matter **29**, 465901 (2017).

[47] A. Dal Corso, Pseudopotentials periodic table: From h to pu, Computational Materials Science **95**, 337 (2014).

[48] J. P. Perdew, K. Burke, and M. Ernzerhof, Generalized gradient approximation made simple, Phys. Rev. Lett. **77**, 3865 (1996).

[49] S. Poncé, E. R. Margine, C. Verdi, and F. Giustino, EPW: Electron–phonon coupling, transport and superconducting properties using maximally localized Wannier functions, Computer Physics Communications **209**, 116 (2016).

[50] A. Togo, L. Chaput, and I. Tanaka, Distributions of phonon lifetimes in Brillouin zones, Phys. Rev. B **91**, 094306 (2015).

[51] A. M. Brown, R. Sundararaman, P. Narang, W. A. Goddard, and H. A. Atwater, Nonradiative plasmon decay and hot carrier dynamics: Effects of phonons, surfaces, and geometry, ACS Nano **10**, 957 (2015).